

The Role of Double-Tentacled Cooperative Kinematics on the Hydrodynamics of a Self-propelled Swimmer

Z. Li, D. Xia[†] and Z. Zhou

School of Mechanical Engineering, Southeast University, Nanjing, Jiangsu, 211189, China

[†]Corresponding Author Email: dxia@seu.edu.cn

(Received September 15, 2022; accepted February 9, 2023)

ABSTRACT

In this study, we proposed an underwater robotic swimmer integrating dual-actuated composite tentacles. We employed overlapping grid technology to manipulate virtual swimmers and performed simulations of incompressible viscous flow. To facilitate the distinction between three driving modes (the reverse, homologous, and interlace modes), the rear flexible module of the swimmer was divided into three components: thigh links, calf links, and caudal fins. The cooperative motion mechanism behind the double-tentacled module exhibited special hydrodynamic properties. Under the same kinematic parameters, the reverse mode exhibited the best energy-saving and propulsion effect, whereas the homologous mode was affected by lateral energy loss, thus resulting in the worst propulsion effect. However, the joint system exhibited anti-interference and spanwise flexibility. The interlace mode produced a certain error in the lateral displacement, and the propulsion efficiency was between the former two modes. Compared with traditional fish-like robots, the diverse actuation morphologies of the swimmer reported in this study exhibit extremely powerful self-propelled functionality, and its key features, including the geometry of an aquatic squid and the kinematics of the stretched body-caudal fin pattern, offer insights into the analysis of self-propelled hydrodynamics.

Keywords: Cooperative kinematics; Double-tentacled swimmer; Driving mode difference; Self-propulsion; Wake structure.

NOMENCLATURE

C_{FAx}	longitudinal force coefficient (homologous)	L_b	body length of the swimmer
C_{FAy}	lateral force coefficient (homologous)	t	transient time
C_{FBx}	longitudinal force coefficient (interlace)	T	swing cycle
C_{FBy}	lateral force coefficient (interlace)	η	propulsion efficiency
C_{FCx}	longitudinal force coefficient (reverse)	θ_{max}	maximum pitch angle
C_{FCy}	lateral force coefficient (reverse)	λ	wavelength
C_{PL}	useless energy coefficient	φ	phase difference between the adjacent links
C_U	average swimming velocity coefficient	$\Delta\alpha$	double-tentacled phase difference
f	swing frequency		

1. INTRODUCTION

The evolution of fish swimming skills can be traced back hundreds of millions of years, and the underwater bionics constructed by the human research community is only a product of modern times (Sfakiotakis *et al.* 1999; Singh *et al.* 2017; Acharya and Casimiro 2020). Therefore, the autonomous underwater vehicle (AUV) is a famous propulsion representative currently active in the field of applied fluid mechanics, and its development is inspired by the mobility of fish (Roper *et al.* 2011; Wynn *et al.* 2014; Singh *et al.* 2019). As an emerging

industry, the bionic fish has broad potential application prospects and is convenient for underwater exploration, military exercises, and resource extraction. Manual remote intervention reduces the chances of human risk-related work and improves the safety and reliability of marine engineering. The research scope of AUVs covers various aspects, such as fish-like shape construction (Leroyer and Visonneau 2005), kinematic modeling (Park *et al.* 2012), energy-saving mechanisms (Xia *et al.* 2018), and moving target tracking (Suebsaiprom and Lin 2015). Inspired by the combination of the original ecological squid shape and the body-caudal fin (BCF) swimming mode, this paper proposes an unexplored compound synergistic

propulsion mechanism. In this numerical work, we simulated the motion of flexible and maneuverable tentacles to verify the feasibility of this self-propelled dynamics. The traditional BCF swimmer can provide the travelling wave propulsion mode, and its corresponding hydrodynamic performance form a systematic theory. This paper presents a new idea: the double-tentacled swimmer provides three driving modes. Unlike the undulating fish, although the tentacles do not interfere with each other, the flow field environment formed is bound to be very complicated. In this paper, we perform an in-depth exploration of the special hydrodynamic properties extended by the law of complex motion.

From the bionics perspective, a fish-like robot that implements the BCF mode is more compatible with the human cognition of water bodies. Previous studies have explained the swimming effect produced by combining a flexible prototype and a single-stiffness caudal fin based on experimental tests (Wu *et al.* 2014; Yu *et al.* 2016) and numerical simulations (Dong and Lu 2005; Yang *et al.* 2011). Compared with the traditional propelling method (Carrica *et al.* 2010; Duman and Bal 2019), the fish-like robot relies on the thrust generated by the multijoint pendulum axis to simulate the movement of fish (Liu *et al.* 2014). The concept of a parallel symmetrical dual-tail robot was first reported in 2000. This robot was operated based on an ion-conducting polymer film actuator (Guo *et al.* 2000). To optimize the control of the fish body, Fetherstonhaugh *et al.* (2021) performed joint linkage processing on the bending points of different types of fish and highlighted the importance of head joints. Liu *et al.* (2020) applied the common linkage mechanism in mechanical systems to fit the tail swing law and simulated the eddy current law in the double-tailed fin mode distributed forward and backward. Yu *et al.* (2007) applied a multichain strategy to robotic fish and obtained an optimized link length. The aforementioned studies provide a comprehensive mechanical understanding based on fish morphology and kinematics. The specific research results are relatively advanced, and the concept of a multitailed robot has recently gained popularity and is in the exploratory stage. Two previous studies developed a miniature bionic fish based on double-tailed fins that can integrate oscillation and jet propulsion, thus focusing on the influence of the distance between the tail fins on swimming stability and mobility. Their systematic experiments confirmed that a reasonable swing law can realize complex movements, such as ascending and turning (Zhang *et al.* 2016; Liao *et al.* 2018). Xie *et al.* (2018) proposed a four-tailed bionic jellyfish robot, which organically combined wave and jet propulsions, thus revealing the influence of a new propulsion concept on hydrodynamics. Coelho *et al.* (2020) studied the propagation law of interface of active nematics on substrates based on microhydrodynamics, revealing the impact of the second flagellum on the bacteria motility. This study also belongs to the category of multi-module movements. Multitailed coordination studies have specific developmental prospects in enhancing the propulsion effect and control performance, and a self-propelled

movement mechanism that depends on multijoint double tails has not been reported.

The beauty of examining the self-propulsion of underwater robots is in the capture of transient decision-making action. In previous numerical studies on self-swimming, the complex kinematics of multiple fishes were coupled in the flow field. In the median and/or paired fin mode, Li *et al.* (2021) employed the immersed boundary method to drive the evolution underwater vehicle with symmetrical pectoral fins and discussed the linear relationship between the forward Reynolds number and roll amplitude. Xu and Wan (2012) applied the overlapping grid method to explore the self-locomotion of rigid pectoral fins, and considered the additional effects of lateral force and moment in the iterative calculation. Su *et al.* (2021) observed that the geometric structure of stingrays could ensure high efficiency during swimming, and the source of their propulsion was the flexible waves of its expanding wings on both sides. In the BCF mode, Li *et al.* (2020) described the kinematics of a deformed puffer fish with multiple fins and highlighted the influence of flexibility on the self-propulsion effect. Feilich and Lauder (2015) adopted the geometric parameters of a tail shape as a variable to examine the effect of wave swimming on the performance of autonomous swimming speed. In our previous numerical investigations (Xia *et al.* 2015, 2018, 2021), we performed systematic studies on the straight line cruise of a single caudal fin in terms of the amplitude of a flexible caudal fin, energy-saving mechanism, and head control. In this study, we systematically analyzed the self-swimming characteristics of a swimmer with dual-actuated tentacles. Note that additional verification is required regarding if the swimmer and the three corresponding motion modes can reproduce the traditional self-propulsion process. However, undoubtedly, this compound underwater propulsion mechanism is a novel breakthrough in the field of AUVs.

Here, an underwater robot with double tentacles and multiple linkages was selected as a motion carrier to study the effect of different driving morphological combinations on self-propulsion. Generally, different from the monotonicity and discriminability of the traditional fish-like waving, the coordination of the two tentacles can exhibit more efficient and variable linear propulsion performance. We emphasized a detailed quantitative method to control the characteristic parameters of multijoint kinematics and obtained the self-swimming law of the bionic robot in a three-dimensional (3D) space via numerical simulations. Consequently, the pressure cloud and 3D vorticity structure attached to the fish body can mathematically explain the contribution of the double-tentacled kinematics to the swimming performance in each driving mode.

2. MATERIALS AND METHODS

2.1 Computational Model and Domain

To ensure the compatibility of the structural frame of

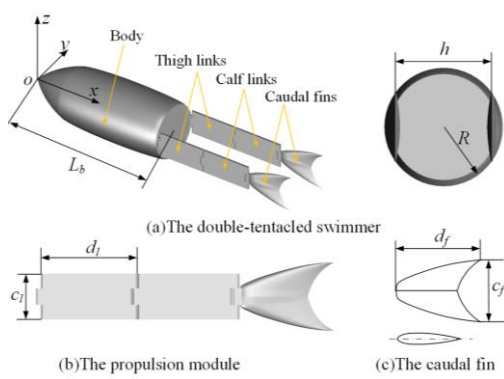


Fig. 1. Geometrical skeleton of the virtual swimmer.

the robotic swimmer with bionics, we designed and optimized a simulation model based on a real squid skeleton (Anderson and Grosenbaugh 2005) in the Cartesian XYZ coordinate system (Fig. 1). Conventionally, the front half of the squid is a streamlined cavity with a water spray mechanism (Rahman *et al.* 2011). The symmetrical fins on both sides provide balance and propulsion. In this study, we simplify the surface of the virtual swimmer, and the model size is controlled using an important parameter called ratio (ε). The geometrical relationship is defined by the following equation: $\varepsilon = L_b/R$, where L_b represents the body length of the swimmer, R is the maximum radius in the transverse direction, and h is the distance between two tentacles (Olcay *et al.* 2017). The second half of the squid usually comprises multiple soft tentacles. Here, we imitate and optimize this half as a multijoint propulsion system. The entire propulsion module includes thigh links, calf links, and caudal fins, every two adjacent links are hinged to facilitate a flexible swing (the details of the screws and nuts in the connecting part are omitted). The link length and width are d_l and c_l , respectively. The joint is constructed as thinly as possible to minimize interference with the surrounding fluid. The mold of the caudal fin is regarded as a symmetrical crescent shape, and the cross-section of the side view of the caudal fin is a NACA0018-type airfoil. The overall aspect ratio of the caudal fin is $A_R = d_f/c_f$, where d_f and c_f denote the fin length and width, respectively. The appropriate aspect ratio and shape of the caudal fin can achieve the optimal propulsion effect.

Based on the dynamic overlap technology, the computational domain is set up comprising the outer zone for realizing the swimmer's transient translation and the inner zone for adapting to the kinematics of the swimmer's body. The two zones are related by overlapping grids. The relevant size and boundary conditions of the swimming area are shown in Fig. 2. The basic physical size of the outer zone is $10L \times 2L$. In Fig. 2, We choose the length of the outer area as $10L$ to ensure that the swimmers have enough forward space, thereby confirming the convergence of the transient speed, while the spanwise space is selected as $2L \times 2L$ to accurately capture the information of wake. The position of the virtual swimmer obtained after the constant iterative calculation is time-controlled during self-motion.

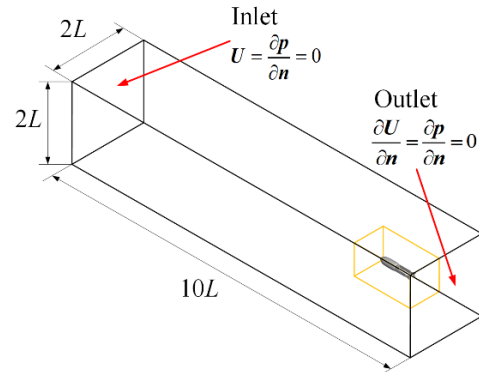


Fig. 2. Details of the computational domain.

The boundary of the swimming area is defined by the upstream inlet, downstream outlet, and far-field part. The specific conditions of the upstream inlet and the far-field boundary are imposed as zero velocity and zero pressure gradients. The boundary condition of the downstream outlet refers to the pressure outlet condition, which is zero velocity and pressure gradients. At the interface between the double-tentacled swimmer and the fluid, we ensure a balance between the fluid and swimmer velocities by imposing a no-slip boundary condition and assume that the standard and tangential velocities of the fluid particles are zero on the surface of the swimmer.

2.2 Kinematics

Figure 3 shows a bionic robot with double tentacles and a multijoint configuration, whose detailed kinematics are used for underwater propulsion. We define the advancing axis (x -axis) along the body length and the lateral axis (y -axis) along the span. Thus, the swimming direction of the bionic robot is along the negative direction of the advancing axis. The entire physical structure could be abstracted into the rigid front and flexible posterior segments. The primary kinematic laws that implement complex actions are concentrated in the posterior segment. Facing the entrance, the left and right tentacles are defined based on common sense. We choose the right tentacle as the main reference object for the study. We abstract the sequence from the leg root to the caudal fin as a three-segment linkage mechanism ($i = 1, 2, \text{ and } 3$). The angles of the linkage relative to the advancing axis are denoted as $\theta_1, \theta_2, \text{ and } \theta_3, (x_i, y_i)$, which refers to the coordinates of each joint

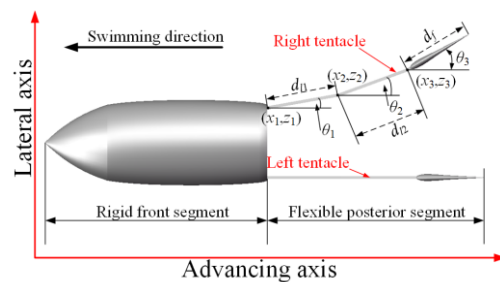


Fig. 3. Schematic of the robot and the basic kinematics of one tentacle.

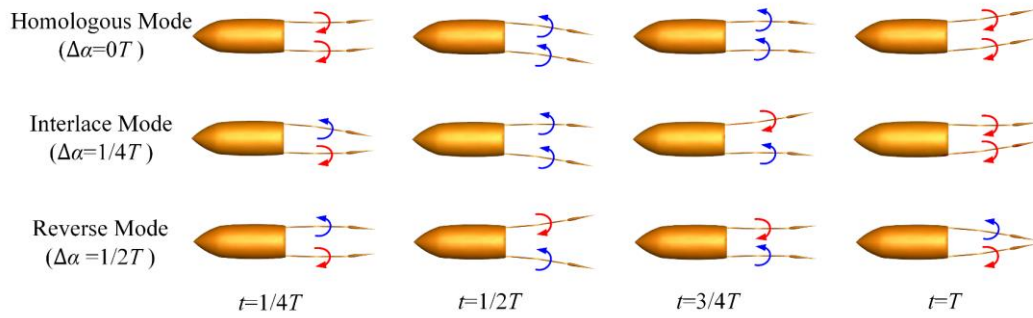


Fig. 4. The schematic laws of three driving modes.

torsion point in the generalized inertial reference system. The motion of each link comprises active rotation and auxiliary heave in the vertical oxy plane to reproduce the kinematic mechanism of the fish-like traveling wave propulsion. Referring to the swing of the traditional caudal fin (Xia *et al.* 2021), we separately describe the motion law of the pitch angle of each joint ($i = 1, 2, 3$) as follows:

$$\theta_i(t) = \sum_{n=1}^i \{h(t) \cdot \theta_{\max} \cdot \sin[2\pi(ft - \frac{\sum_{l=1}^{i-1} d_{l(i-1)})}{\lambda} - (i-1) \cdot \varphi]\} \quad (1)$$

where θ_{\max} is the maximum pitch angle, f is the unified swing frequency, λ is the unified wavelength, φ is the phase difference between the adjacent links, and $h(t)$ is the time-varying control function in the entire simulation process, which is briefly described as follows:

$$h(t) = \begin{cases} \frac{t-t_0}{t_1-t_0} - \frac{1}{2\pi} \sin(2\pi \frac{t-t_0}{t_1-t_0}) & t < t_1 \\ 1 & \text{if } t \geq t_1 \end{cases} \quad (2)$$

where t_0 is when the swimmer has just begun to swing from a stationary state, and t_1 is when the swimmer has just begun to swing in a steady state. We define the interval between t_0 and t_1 as the preparation time for stable propulsion. When the transient time, t , exceeds t_1 , the value of $h(t)$ is equal to 1, indicating that the swimmer's kinematics shows a regular traveling wave swing at this time and was no longer affected by the time-varying control function.

The essence of cooperative swing behavior is that the double-tentacled movement creates several possibilities in the field of complex motion. After defining the basic working mechanism of the single tentacle, we first obtain three linear driving modes (homologous, interlace, and reverse modes) according to the deflection law of the two tentacles. We define a new kinematic parameter named the double-tentacled phase difference, $\Delta\alpha$, to mathematize the cooperative relationship between the two swing tentacles. The cooperative relationship model between the two tentacles can be obtained by extending Eq. (1): $\theta_{ri}(t) = \theta_{li}(t + \Delta\alpha)$, where $\theta_{ri}(t)$ and $\theta_{li}(t)$ represent the transient deflection angles of the

i -th joint of the right and left tentacles, respectively. As shown in Fig. 4, the swimmer use the undulating motion of the three joints in the back half of the body to obtain a symmetrical forward thrust in one swing cycle T . The clockwise red and counterclockwise blue pointers represent the moments when the tentacles are swinging downward or upward at the corresponding moment, respectively. When $\Delta\alpha$ is 0 T , the two tentacles are highlighted using the law of consistency, showing the same traveling wave rule, which is the homologous mode. When $\Delta\alpha$ is $1/4$ T , the sinusoidal fluctuation of the left tentacle is a quarter of a cycle faster than that of the right tentacle. The cross-fluctuation of the two tentacles produces a symmetrical thrust within one cycle, similar to the traditional freestyle stroke. The double-tentacled swimmer behave in interlace driving mode. When $\Delta\alpha$ is $1/2$ T , a series of swinging actions of the left and right tentacles are precisely mirrored on the oxz plane. This driving mode with symmetrical swing law is called reverse mode. The visualization form is that at each instant, two tentacles are attached to a pair of red and blue pointers in opposite directions. Hence, we define this special form as the reverse mode.

3. COMPUTATION METHOD

3.1 Governing Equations

We adopt the noncharacteristic governing equations to guide the viscous flow covered on the double-tentacled robot. The main theoretical foundations are the Navier–Stokes incompressible equation and the mass conservation equation, which are expressed by:

$$\nabla \cdot \mathbf{u} = 0 \quad (3)$$

$$\rho \frac{\partial \mathbf{u}}{\partial t} + \rho(\mathbf{u} \cdot \nabla) \mathbf{u} = -\nabla p + \mu \nabla^2 \mathbf{u} \quad (4)$$

where ∇ is the gradient operator, ρ is the fluid density, p is the pressure, and μ is the dynamic viscosity. To solve the equations in a domain containing a 3D swimmer moving with prescribed kinematics, the no-slip condition is required to be imposed on the moving boundary with the fluid speed, \mathbf{u} , and the swimmer speed, \mathbf{u}_r , as follows:

$$\mathbf{u}_T = \mathbf{u} \quad (5)$$

Conventionally, any swimming motion of a 3D flexible fish can be described as the sum of a rigid body motion and a deformation motion. In this study, Newton's equations of motion are applied as the theoretical basis for the double-tentacled swimmer, so the spatial motion in the instantaneous iterative process is described as:

$$m \frac{d\mathbf{u}_T}{dt} = (\mathbf{F}_x, \mathbf{F}_y, \mathbf{F}_z) \quad (6)$$

$$J \frac{d\omega}{dt} + \omega \frac{dJ}{dt} = M_z \quad (7)$$

where $(\mathbf{F}_x, \mathbf{F}_y, \mathbf{F}_z)$ represents the flow forces working on the swimmer body along the advancing, pitching, and lateral directions in the space; M_z is the flow moment acting on the swimmer body in the z -axis direction; m is the mass of the virtual swimmer; ω is the rotating angular velocity; and J is the moment of inertia of the rotating pivot. Moreover, we express fluid forces and moments based on the theory of fluid dynamics as follows (Kern and Koumoutsakos 2006):

$$(\mathbf{F}_x, \mathbf{F}_y, \mathbf{F}_z) = \int_S \boldsymbol{\sigma} \cdot \mathbf{n} dS \quad (8)$$

$$M_z = \int_S [(\boldsymbol{\sigma} \cdot \mathbf{n}) \times (\mathbf{x} - \mathbf{x}_c)] \cdot \mathbf{e}_z dS \quad (9)$$

where $\boldsymbol{\sigma}$ is the stress tensor, \mathbf{n} is the unit vector along the normal direction, dS is the differential unit area of the force surface, and \mathbf{e}_z is the unit vector along the z -axis.

3.2 Overset Grid Method

The dynamic overset grid method can enable the grid system to follow the rigid reference body to realize autonomous movement, and the boundary of the overlapping area exhibits the flexibility to adapt to any direction. This technology to simulate and integrate complex motion systems has been widely applied in the field of fluid mechanics, including underwater robots and ship engineering (Carrica *et al.* 2007; Jiang *et al.* 2019; Ohashi *et al.* 2019; Wang and Wan 2020).

The special boundary processing of overlapping grid technology can considerably reduce the difficulty and workload of data transmission between subregions. The relative movement between the subdomains does not require grid deformation or regeneration. It is extremely convenient to adopt dynamic overlapping grids for complex structures with relative motion. As shown in Fig. 5, the entire calculation area can be discretized into a background grid surrounding the entire solution domain and a body-fitting grid covering the bionic swimmer (a suitable cube box). The rectangular background domain is constructed as a structured hexahedral grid

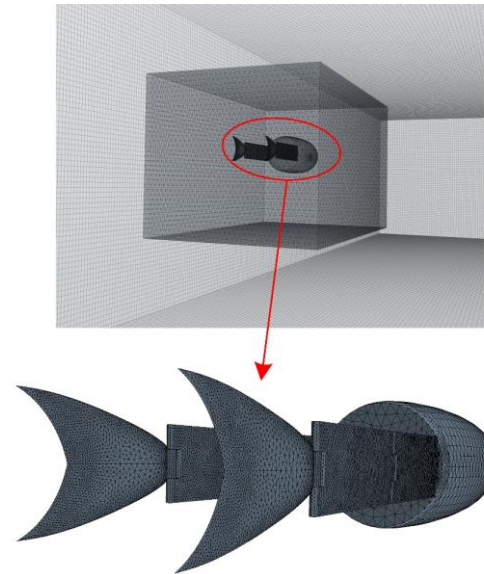


Fig. 5. Detailed display of the overlapping grids of this study.

to capture the rigid motion of the six degrees of freedom (DoFs) parameters, and the volume in the cube is discretized into an unstructured tetrahedral grid, which can adapt to a wide range of deformations. To capture complex flow characteristics, local mesh refinement is performed near the robot to ensure that the multijoint deformation function was satisfied.

3.3 Numerical Method

To obtain high-quality simulation results, we employ the overlap calculation tool in the commercial software package, Ansys Fluent, to solve the flow problem. This package is widely used to confirm the space-time finite volume method and discretize the Navier–Stokes control equations. In addition, it is widely applied in various complex and representative hydrodynamic environmental studies. Doustdar and Kazemi (2019) simulated the overturning conditions of damaged ships in regular beam waves based on the sliding interface and dynamic layering technologies in the solver, Fluent. Moreira *et al.* (2020) numerically verified the propulsion performance and energy recovery in marine engineering equipment based on the double-flapping wing system. In our previous study, Fluent, as an advanced transient solver, simulated the wall adjustment function of the flexible deformation of the fish-like robot (Xia *et al.* 2015, 2018, 2021).

The specific settings of the simulation for this study are as follows: the Green–Gaussian element method is employed for the gradient interpolation, the second-order upwind scheme is selected for the convection term, and the second-order implicit scheme is applied for the transient formation. The pressure–velocity coupling of the continuity equation is realized using the SIMPLE algorithm. The flexible posterior segment can be divided into multiple rigid body parts in the implementation of specific motion iterations. Commonly, such case

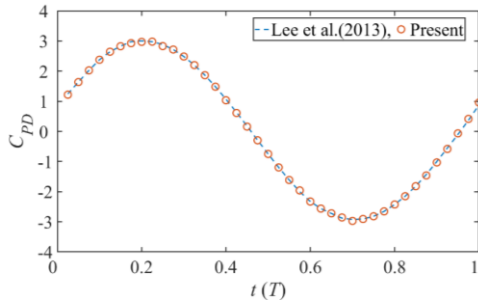


Fig. 6. Comparison between the present simulation scheme and that of Lee and You (2013) on the pressure drag coefficient, C_{PD} , of a moving sphere in a single cycle.

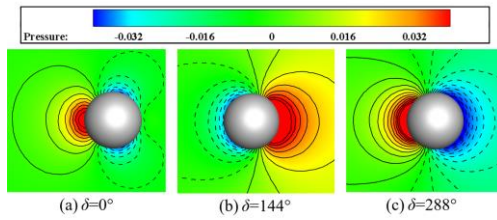


Fig. 7. Profile of the instantaneous pressure on the moving sphere (the phase differences were 0° , 144° , and 288°).

descriptions can be implemented by compiling the DEFINE_CG_MOTION macro and user-defined function (UDF). UDF complements the built-in functions and can meet more computational needs by tuning quantitative parameters. To obtain more accurate results based on the calculation cost, we control the time step $dt = 0.005T$. For each step, smoothing and remeshing methods are employed to regenerate the meshes used for iterative calculations.

The self-propelled simulations are configured with a constant fluid viscosity of $\mu = 1.01 \times 10^{-3}$ Pa·s and a fluid density of $\rho = 1.0 \times 10^3$ kg·m⁻³. According to the calculations of the self-propelled velocity increasing from zero to a constant value and the constant length of the double-tentacled swimmer, Re is roughly between 0 and 10^4 . Under the condition that the value of Re is transient, a feasible method may be to use the transition system to conduct systematic research.

3.4 Numerical Validation

A numerical method that has been accurately verified is a prerequisite for simulation. Based on the theoretical basis in the previous section, we reproduced the simple harmonic oscillation law of a single-DoF sphere in stagnant water. The size of the 3D sphere and the environment of the flow field were strictly referred to in authoritative papers by Lee and You (2013) and Seo and Mittal (2011). As shown in Fig. 6, after comparing and analyzing the verification results with the simulation data of Lee and You (2013), we observe that the present calculated results of pressure components are extremely close to those of the previous studies. Figure 7 indirectly and

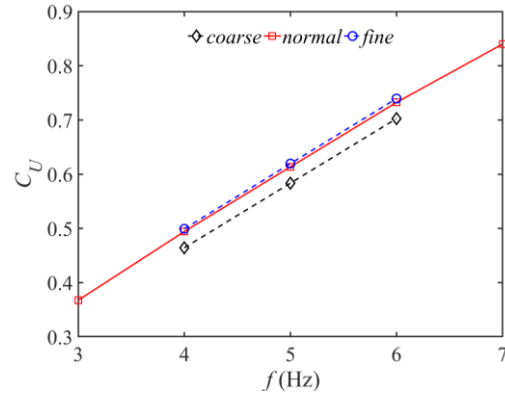


Fig. 8. Grid sensitivity test.

visually verifies the correctness of the numerical method from the perspective of a pressure cloud chart. Based on three different phase differences, the pressure difference contour attached to the 3D sphere is almost the same as that of Lee and You (2013). Compared with the results obtained by Lee and You (2013), the validation in the our study uses a color display to represent the overall characteristics of the flow through the sphere, showing the instantaneous profile along the spanwise vorticity, thereby visualizing the data shown in Fig. 6.

The grid convergence test was conducted by distinguishing different uniform side lengths of 0.016, 0.008, and 0.004 L_b in this study. The corresponding grid numbers were 1.2 (coarse), 5.3 (normal), and 12.5 (fine) million, respectively. To standardize the quantitative grid convergence verification, we unified the relevant settings of the computational domain and boundary. In addition, we selected the homologous mode as the reference object and unified the kinematic quantification parameters configured on the double-tentacled swimmer except for the swing frequency, f . The value of f was controlled within a range of 3–7 Hz. Figure 8 shows the dimensionless mean swimming velocity, C_U , of three grid sizes as a function of f . Notably, under the same parameter conditions, the swimming law simulated using the coarse grid had an error, whereas the normal and fine grids could better deal with the hydrodynamic problem of double-tentacled cooperative behaviors. A normal mesh discretization region with a size of 0.008 L_b was an appropriate scheme for this study.

3.5 Behavior Parameterization Method

Using the standard kinematic equations, the double-tentacled swimmer can achieve three driving modes of locomotion. To quantitatively describe such diversified movements, we use various dynamic measurement parameters to describe underwater work. Figure 9 shows the decomposition and integration diagram of the main driving parameter, $F_i(t)$, under the numerical scheme. Specifically, we define the force parameters of the three different states as $F_{A_i}(t)$, $F_{B_i}(t)$, and $F_{C_i}(t)$. Subscripts A, B, and C represent the three movement modes shown in Fig. 4 ($\Delta\alpha = 0 T$, $1/4 T$, and $1/2 T$, respectively). e_j is the

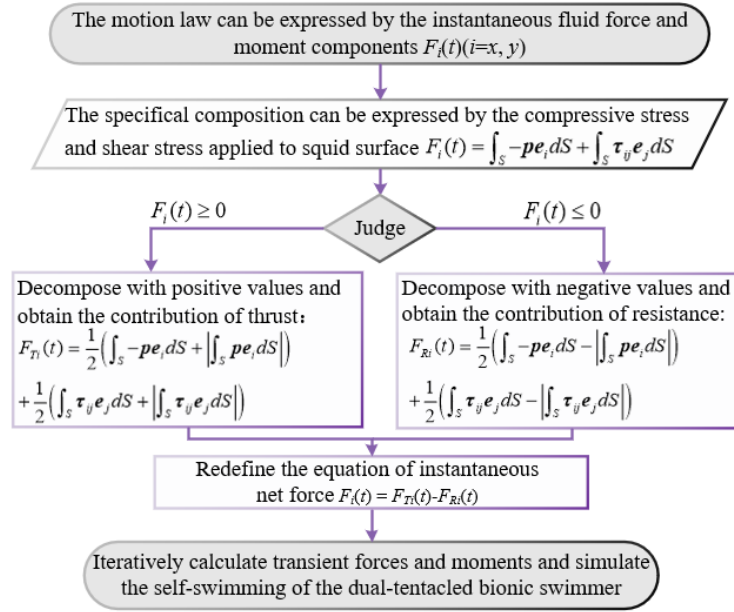


Fig. 9. Decomposition and integration diagram of the main driving parameter, $F_i(t)$, under the numerical scheme.

division of the normal vector of the robot unit surface, and τ_{ij} is the viscous stress tensor for dual-actuated linear propulsion. Based on the governing Eqs. (3) and (4), we decompose the value of $F_i(t)$ of the periodic changes in different directions of motion and summarize them into two groups (positive and negative).

To instantaneously compare the advantages of the three different forms of propulsion, we formulate dimensionless expressions of the instant velocity and force with a function of t along the longitudinal and lateral directions as follows:

$$\begin{bmatrix} u_{Ax}(t) & u_{Ay}(t) \\ u_{Bx}(t) & u_{By}(t) \\ u_{Cx}(t) & u_{Cy}(t) \end{bmatrix} = \begin{bmatrix} \dot{x}_A(t) & \dot{y}_A(t) \\ \dot{x}_B(t) & \dot{y}_B(t) \\ \dot{x}_C(t) & \dot{y}_C(t) \end{bmatrix} \cdot \frac{T}{L_b} \quad (10)$$

$$[C_{FAi} \quad C_{FBi} \quad C_{FCi}] = \frac{[F_{Ai}(t) \quad F_{Bi}(t) \quad F_{Ci}(t)]}{0.5\rho U^2 L_b^2} \quad (11)$$

The swimmer inevitably produce vertical movement along the y -axis direction and roll movement around the z -axis when moving forward. We believe that the energy consumed by these two movements in the process of propulsion is useless. The following universal energy-related equations are obtained by analogy for the three driving modes. The dimensionless useless power consumed by the swimmer to overcome the fluid reaction can be expressed as follows:

$$P_L = F_y(t) \cdot \dot{y}(x, t) + M_z(t) \cdot \omega(x, y, t) \quad (12)$$

$$C_{PL} = \frac{P_L}{0.5\rho U^3 L_b^2} \quad (13)$$

To quantify the propulsion effect, the Froude efficiency (Schultz and Webb 2002) calculation is introduced here as:

$$\eta = \frac{\bar{F}_{Tx}(t) \cdot U}{\bar{F}_{Tx}(t) \cdot U + \bar{P}_L} \quad (14)$$

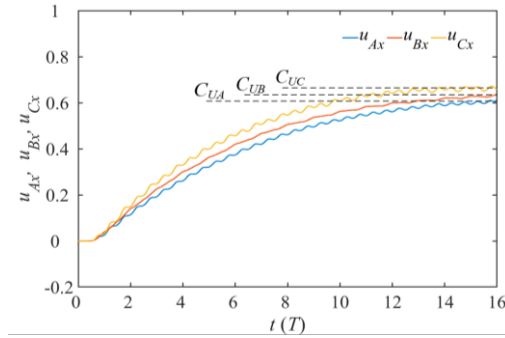
where U denotes the stable-state cruising velocity, and $\bar{F}_{Tx}(t)$ and \bar{P}_L are the average thrust force and average useless power during one cycle, respectively. The dimensionless stable-state cruising velocity is determined by $C_U = U^*T/L_b$.

4. RESULTS

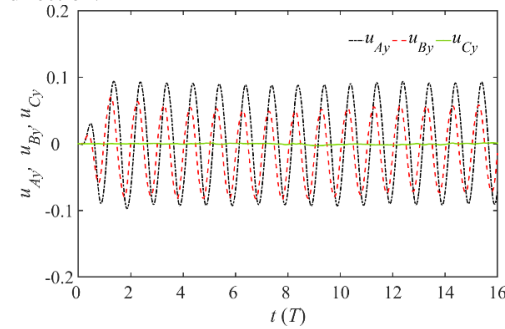
In this study, we reconstructed the complex geometry and specified the motion of tentacles in terms of conceptual dimensions. Finally, we calculated the swimmer's self-propelled response based on net hydrodynamic forces.

4.1 Time History Variations in Performance Parameters

During the evolution of self-swimming behavior, the speed and strength of the biomimetic swimmer show noticeable unsteady changes. The operation stroke of the flexible rear segment stimulates the fluid environment, making the flow field around the rigid body change qualitatively, and the feedback of the flow field also reflects on the body surface, so that the swimming visualization gradually tends to balance. Figure 10(a) shows the time history of the instantaneous swimming velocity coefficients (u_{Ax} ,



(a) Time history curves of the transient velocity coefficients of the three modes along the forward direction.



(b) Time history curves of the transient velocity coefficients of the three modes along the lateral direction.

Fig. 10. Comparison of the velocity coefficients of the three driving modes.

u_{Bx} , and u_{Cx}) obtained with unified performance parameters in the three driving modes. The specific kinematic parameters are the swing frequency $f = 5$ Hz, and the maximum pitch angle $\theta_{max} = 15^\circ$. At $t = 0$, the swimmer and fluid are at rest. When the robotic swimmer begins by command and moderately accelerates, the fluid undergoes a transient process and gradually stabilizes (critical values C_{UA} , C_{UB} , and C_{UC} are obtained). Figure 10(a) shows that the curvilinear convergence tendencies of the three modes are similar; the gap between the three curves first expands and then shrinks over time. This asymptotic average curve law is similar to the reported numerical simulation results of a single caudal fin (Borazjani and Sotiropoulos 2010; Feng *et al.* 2020), confirming the effectiveness of the proposed mechanism. Moreover, the fluctuation diversity is worth considering. The velocity history (blue line) of the homologous mode has analogous results similar to the self-propulsion of a bionic tuna prototype, only with a certain difference in the amplitude of the fluctuation (Xia *et al.* 2015). The reverse mode is superior to the other modes, having the fastest starting acceleration and the highest final steady-state velocity coefficient, C_{UC} . In one swing cycle, the amplitude of every two adjacent peaks or valleys is uneven. The reason behind this can be interpreted by the vorticity distribution law. The convergence characteristic of the interlace mode (orange line) is an extremely smooth transition, which could be understood as follows: the effect of the cross-phase of the advancing peaks and valleys in a single cycle is smoothed and offset.

Figure 10(b) shows the time history of the instantaneous lateral velocity coefficients (u_{Ay} , u_{By} , and u_{Cy}) in the three modes. For the homologous mode, u_{Ay} abruptly increases from 0 at birth and alternately fluctuates around 0 with a constant amplitude of 0.09, which can be understood as in the self-propulsion process, where the center of mass (COM) exhibits a certain horizontal movement instead of maintaining a straight line. This phenomenon also agrees with the traditional traveling wave propulsion, but the difference is that the double-tentacled model can aggravate the lateral displacement component. The reverse mode produces almost no lateral displacement in the entire process, and the characteristic root of the curve is infinitesimal and accompanied by a small wave point. This is because the kinematics of the left and right tentacles are completely symmetrical about the oxz plane, subtly offsetting unnecessary lateral work. The interlace mode in the y -axis exhibits asymmetrical lateral movement, and it continuously moves sideways in the negative direction of the y -axis with a small magnitude. This shows that when $\Delta\alpha = \frac{1}{4} T$, the self-propulsion is not simply along the advancing direction. The swimmer is confirmed to generate lateral fluctuations and incremental displacement errors that deviate from the original track during the entire process from the beginning to convergence.

When the swimmer achieves self-propulsion to begin in situ, the transient force attached to its surface depends on the relative motion between the rigid body and the surrounding flow field environments. As reported by Carling *et al.* (1998), in the absence of external forces, an organism can tend toward an asymptotic state after several cycles. Under the guidance of the three kinematic methods (Fig. 4), we divided the time-varying force of the three working conditions into two direction components based on the simplified concept (the force in the z -direction is very insignificant and, therefore, negligible). The performance details of the combined force law acting on the double-actuated swimmers exhibit diversity, specifically expressed as the longitudinal force coefficients (C_{FAx} , C_{FBx} , and C_{FCx}) and lateral force coefficients (C_{FAy} , C_{FBy} , and C_{FCy}) (Fig. 11). We define the forward direction as along the negative x -axis, i.e., the negative value represents the promoted thrust generated on the swimmer. When the negative magnitude is sufficiently large, the underwater body

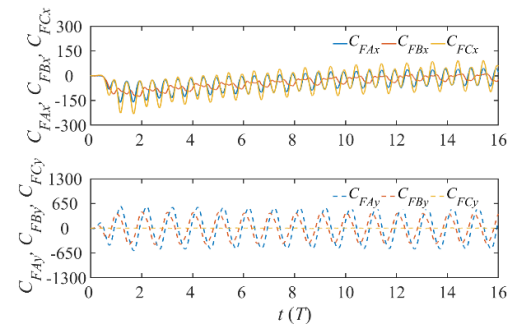


Fig. 11. Comparison of force coefficients of the three driving modes.

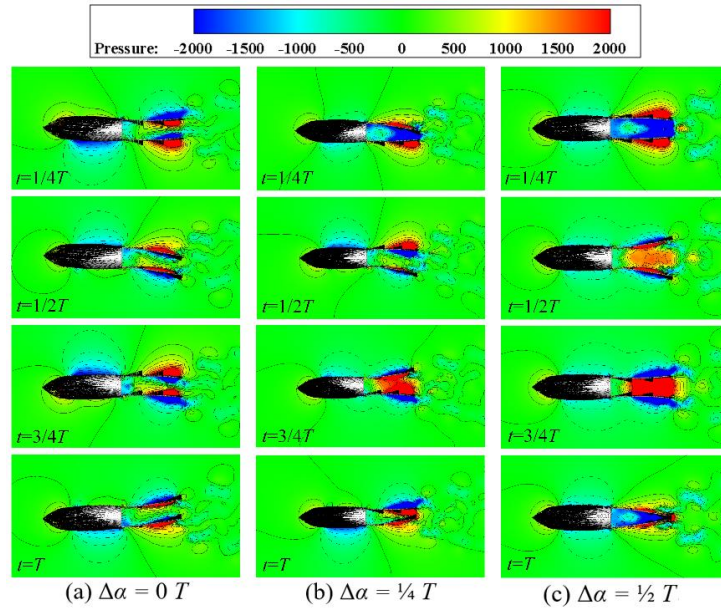


Fig. 12. Pressure contours and velocity vectors of the bionic swimmer at different $\Delta\alpha$ values.

is in the acceleration stage. As shown in Fig. 11, in the time interval from 0 to $8T$, the average longitudinal force coefficients of the three driving modes are -53.75 , -58.04 and -62.43 . In the later stage, the three types of swimmers are in the fluctuation stage of positive and negative balance, indicating that the swimmer has completed the autonomous propulsion and is in the cruising posture. Regarding the details of the difference among the three curves, the longitudinal force coefficient of the homologous mode, C_{FAx} , is a stable sine convergent wave, whereas that of the reverse mode, C_{FCx} , is a unique sine convergent wave with staggered peaks. This difference directly explains the change law of the advancing velocity coefficient shown in Fig. 10. There is no prominent peak in the longitudinal force coefficient of the interlace mode, C_{FBx} , and the performance curve is more like a flattened mountain. This is because the left and right tentacles have an effect due to the cross-fluctuation regularity. Similar to the flow of people at the wrong peak, the average propulsion force value during the cycle exceeds that of the homologous mode blocked in the peak period. Fig. 11 shows the lateral force coefficients (C_{FAy} , C_{FBy} , and C_{FCy}) of the three driving modes. The lateral force coefficients of the homologous and interlace modes fluctuate around zero from the beginning. Thus, we can reasonably infer that the maximum amplitude of the positive and negative values of the stabilized C_{FAy} should be close, and the maximum value of the negative value in the C_{FBy} curve should slightly exceed that of the opposite value. The value of C_{FCy} is approximately a straight line, indicating that the swimmer in this driving mode can effectively restrict lateral movement.

4.2 Transient Variation of the Flow Field

Figure 12 shows the pressure distribution and velocity vectors of the three driving modes (different

$\Delta\alpha$ values). The pressure distribution is expressed in contours and color gamut, whereas the velocity vectors are described in dense arrows.

First, we conduct a systematic analysis of the pressure distribution of the three modes. For the homologous mode ($\Delta\alpha = 0 T$), the distribution of the red high-pressure core and blue low-pressure core attached to both sides of the two tentacles is consistent, correlating with the alternating pressure law of the traveling wave swing of a fish tail (Borazjani *et al.* 2012; Xia *et al.* 2015). The present findings show that the difference is that the right tentacle of the interlace mode moves faster than the left tentacle by a $\pi/2$ phase difference. When $t = 1/2 T$, the left tentacle is in the extreme position, and the front and back surfaces are marked as fast-dissipating pressure cores. The precise moment shows that the left tentacle has just completed the final stage of half of the journey, whereas the right tentacle is in the sprinting stage of the right pendulum. The arc range of the accompanying pressure core is large and full, indicating that the swing of the right tentacle at this moment produces an enormous pressure difference and is the main driver. When $t = 3/4 T$, the left tentacle is the main driver, and the right tentacle is in the extreme position. The other two stages can be deduced by analogy. This alternate pressure differential format is the primary feature of the interlace mode. The pressure distribution of the last reverse mode is axisymmetric. When $t = 1/4 T$, the left and right tentacles rapidly expand to the outside, and both sides reach the limit position at $1/2 T$. At $t = 3/4 T$, the left and right tentacles rapidly contract to the inside, and the water on the inside is squeezed and gradually merges to form a complete red high-pressure core. This moment provides swimmers with a driving thrust greater than those of the other two modes. Moreover, this is also the reason for the higher peak in the periodicity shown in Fig. 11. When $t = T$, the two tentacles begin to swing outward again. The

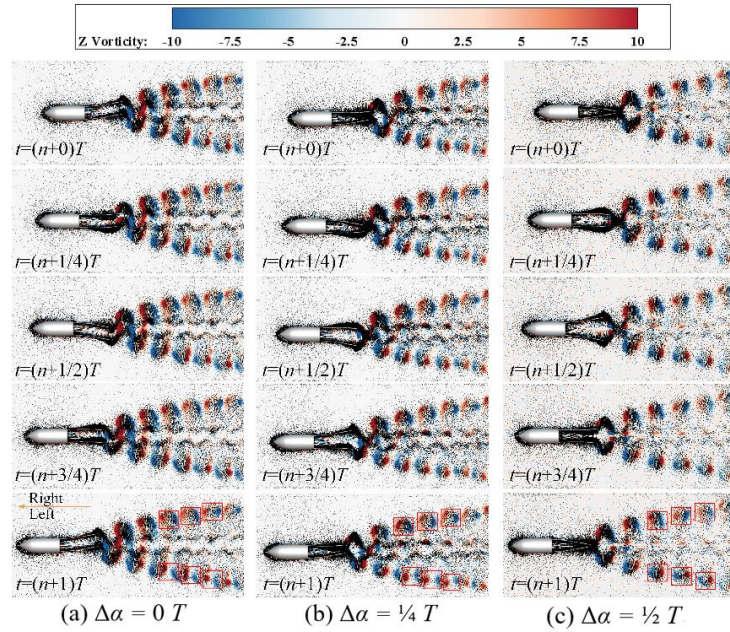


Fig. 13. Vorticity contours of the bionic swimmer at different $\Delta\alpha$ values.

water in the interval has already shown a tendency to considerably flow out after the previous squeeze, and a low-pressure area is formed between the two tentacles. A careful study reveals that a slight symmetrical blue low-pressure area is formed on both sides of the swimmer's body in the reverse mode, whereas the blue low-pressure area of the other two modes is time-related. In the latter, the transfer of the blue dashed line equivalent low-pressure area along the forward direction of the body is affected by the side shift and roll phenomenon. For example, when $t = 1/4 T$ and $t = T$, the blue dotted line equivalent low-pressure area is on the left side of the body, and the swimmer tends to move sideways to the right.

Second, we analyze the law of velocity vector variation. As per a previous study on double-tailed reverse propulsion, the velocity vector was used to describe the tail vorticity, and we innovatively discovered the velocity vector law of the dependent drive source (Liao *et al.* 2018). For the homologous mode, the velocity vector arrow on the front edge of the swimmer's body is not straight along the forward direction. With the lateral displacement and roll in one cycle, the speed vector direction fluctuates from diagonally upward to diagonally downward. This corresponds to the phenomenon in the low-pressure area with the blue dotted line above. The conclusions of side shift and roll are also applicable to the interlace mode, whereas the velocity vector arrow of the reverse mode is always along the forward direction. This indirectly explains why there is no y -axis displacement and force in this mode (Fig. 11). Usually, the arrow points from the swimmer's surface to the outside, representing the direction of the velocity vector, and the arrow length represents the magnitude of the velocity. Regardless of the mode, the arrow fields on the three joints of the swimmer's flexible back segment are gradient distributions of right-angled triangles with different

heights. The reason behind the formation of the triangular shape is based on the following equation: $v_{ix} = \theta_i(t) \cdot d_l$. The linear velocity (v_{ix}) of any point on the i -th link changes in proportion to the instantaneous angular velocity, i.e., the length of the arrow symbolizing the speed value increases linearly. We take the right tentacle in the same driving mode as an example to analyze the changes of the three joint velocity vectors in one cycle. When $t = 1/4 T$, the root of the thigh link is fixed on the body; therefore, the length of the vector arrow is very small, which can be regarded as the vertex of a triangle. There is a phase difference among the three linkages, which is mainly why the right triangle of the calf link is short, and the caudal fin does not even have a velocity vector difference. The arrow image of the velocity vector is exploited to analyze the swing law of each linkage and examine the behavior logic behind the traveling wave propulsion based on the finite volume theory.

Figure 13 shows the evolution of the vorticity contours and vectors at each representative moment in the self-propulsion process of the three modes. Compared with the tail feature results obtained by Liao *et al.* (2018), the present findings also reveal the structural features of the entire downstream flow field. The red and blue blocks serve as the vortex in the counterclockwise and clockwise directions, respectively, and the dense area with black arrows represents the vector distribution. In the time interval from 0 to $1/2 T$, for the reverse mode, a pair of red vortices gradually emerge from the trailing edge of the swimmer's tail to replace a pair of blue vortices that have fallen off. In the homologous mode, the swimmer produces a pair of vortex structures with opposite colors. The situation of the interlace mode is more complicated. Affected by the phase difference between both tentacles, one tentacle may have been in the stage of forming a wake vortex, and the vortex on the other tentacle may have been in the

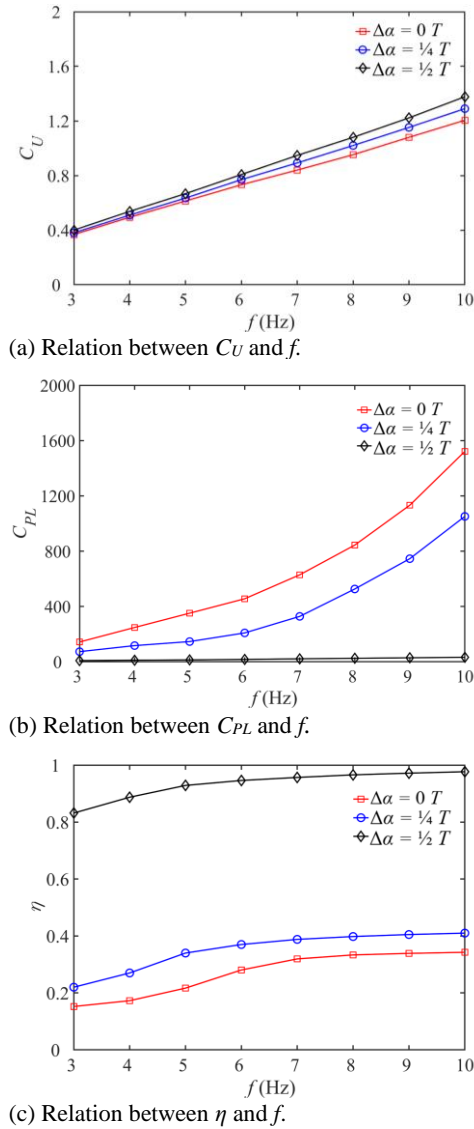


Fig. 14. Relation among C_U , C_{PL} , η , and f based on the three modes.

shedding stage. The phenomenon generated in the time interval from $\frac{1}{2}$ to $1 T$ is similar to that in the first half; therefore, it is not repeated in this section.

To summarize, the vortex-shedding law of single tentacles is similar to that of a reported BCF (Xia *et al.* 2015), and the details of the vortex street of double-tentacle arrangements are unprecedented. The three modes can produce regular vortex street patterns downstream, including two rows of main vortex streets distributed on both sides and two rows of auxiliary vortex streets sandwiched in between. The excessively fast dissipation rate and the relatively small form of the auxiliary vortex street are not convenient for the present analysis, and the specific details of the main vortex street can be distinguished according to kinematics. Here, we consider $t = 1 T$ as an example to characterize the laws of three different vortex streets. When $\Delta\alpha = 0 T$, the kinematics of both tentacles are the same; thus, the vortex street shapes on the left and right sides are completely axisymmetric in terms of color and distribution shape. When $\Delta\alpha = \frac{1}{4} T$, the vortex street

on the right side is utterly axisymmetric in shape, but the vortex color is the opposite. When $\Delta\alpha = \frac{1}{2} T$, affected by the lateral displacement on the left side, the distance between each pair of vortices falling off the left tentacle is smaller than that falling off the right tentacle. The law of cross-oscillation leads to a phase difference between both vortex pairs rather than the above completely axisymmetric features.

4.3 Effect of Kinematic Parameters on Self-Propelled Performance

Our aim is to achieve a bionic prototype with a symmetrical double-tentacled system. The self-propulsion in still water driven by the virtual carrier required quantitative evaluation. Inspired by authoritative studies on self-swimming (Borazjani and Sotiropoulos 2010; Xia *et al.* 2015), we select the average swimming velocity coefficient (C_U), useless energy coefficient (C_{PL}), and propulsion efficiency (η) to investigate the gain or loss caused by the variations in kinematic parameters.

First, we perform variable-frequency parametric simulations for swimmers in the three driving modes (the swing frequency (f) increased from 3 to 10 Hz) to highlight the impact of the double-tentacled phase difference superimposed swing frequency on the contribution of propulsion. Fig. 14(a) plots the change in C_U as a function of $\Delta\alpha$ and f . For the double-tentacled kinematics of a fixed mode, as f monotonously increases from 3 to 10 Hz, C_U exhibits a constant linear-rate growing pattern. The reverse mode has the largest rising slope, followed by the interlace and homologous modes. Inevitably, as the frequency increases, the difference in the C_U values of the three modes becomes more indisputable. Regarding the variation in C_{PL} with $\Delta\alpha$ and f (Fig. 14(b)), we distinctly observe that the three swimmer modes expand the dissipation of useless energy to varying degrees as f increased. Among them, the curve corresponding to the homologous mode increases at an alarming rate, whereas that of the reverse mode appears calm in terms of energy loss. The basis behind this law is that the kinematics of the reverse mode is symmetrical along the oxy plane, which avoids the loss of the fish body in the lateral translation as much as possible, and the rare energy loss is distributed only in the swing of the joints in the flexible rear section. Compared with that in the homologous mode, the regulation of the loss curve in the interlace mode is not as exaggerated as the former, but the swimmer's cross-motion can cause the fish to periodically roll along the z -axis. This kind of energy that is uncondusive for driving propulsion could not be ignored and increases with rising frequency.

To demonstrate the influence of the variable-frequency law on the propulsion contribution, Fig. 14(c) shows the relations of η and f based on different modes. Among them, the propulsion efficiency (η) of the reverse mode is close to 1, matching the fastest propulsion speed (Fig. 14(a)) and the lowest energy loss (Fig. 14(b)). When we consider only the frequency conversion, this mode is

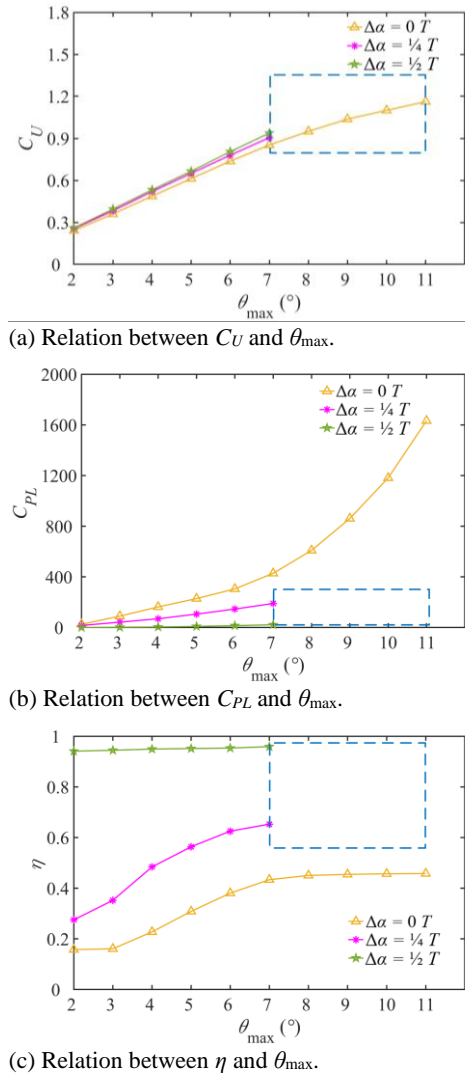


Fig. 15. Relation among C_U , C_{PL} , η , and θ_{max} based on the three modes.

the best propulsion form that double-tentacled swimmers can provide. Careful observation demonstrates that the propulsion efficiency values of the interlace and homologous modes are less than half of that of the former. We believe that the lateral displacement and wave rolling of the fish body absorbs enormous useless energy. Although the overall trend of η shows a curved shape that converges after an increase, the curve can be analogized to an S-type growth model under the influence of different motion phase differences, in which a hidden critical point is defined as the focus of positive and negative growth rates. When $\Delta\alpha = 0 T$, the trend begins from 3 Hz and is in the convergence stage where the growth rate gradually declines. When $\Delta\alpha = \frac{1}{4} T$, the slope of the growth rate first increases and then decreases, and the frequency of the critical point is 4 Hz. Similarly, when $\Delta\alpha = \frac{1}{2} T$, the critical point of the change in the rate of increase slope is the frequency of 5 Hz. The η of different forms nonmonotonously changes, and the reverse mode is better than the other two modes as f increases, and is the first to achieve a parameterized combination with the best propulsion contribution. Thus, under the variable-frequency

quantitative study, the reverse mode is the optimal solution in terms of the propulsion effect, whereas the homologous mode is the worst.

Figure 15 shows the basis of the correlation curve and describes the quantification process of another important kinematic parameter to weigh the propulsion effect. The varying trends of the three evaluation parameters shown in Fig. 15 are similar to those shown in Fig. 14. In the effective range, the increase in the swing angle enhances the propulsion effect. Here, the simulated data is incomplete because of the limitation of the model. The specific details are reflected in the blank part marked by the blue box in Fig. 15. The embarrassing situation is based on the slender body shape of the bionic swimmer. The value of the spanwise radius (R) shown in Fig. 1 should not be extremely large, and the small spanwise space is only suitable for the homologous mode. The other two modes are affected by the excessive pitch angle at certain moments, which can cause interference at the tip of the caudal fin. Figure 15 shows the law of C_U , C_{PL} , and η as a function of $\Delta\alpha$ and θ_{max} . As θ_{max} changes from 2° to 7° , the C_U of the three modes linearly increases. The difference is that when θ_{max} exceeds 7° , although the speed trend of swimmers with the two homologous tentacles is still upward, the growth rate gradually descends as θ_{max} increases. Correspondingly, C_{PL} exhibits a gradual uptrend in the growth rate from 2° to 7° at a given $\Delta\alpha$. When θ_{max} exceeds 7° , the gradual change in the growth slope is assigned a linear monotonic characteristic. This is because as the stacking of each link's pitch angle increases, the amplitude of each corresponding tail also rises. The increase in the effective area of the backward water jet and the ineffective lateral component is also driven. For the propulsion efficiency, the value of θ_{max} has almost no effect on the work of the reverse mode, and the effect on the interlace mode is that as θ_{max} grows, the value of η gradually converges. The homologous mode has the most far-reaching impact, and its curve is analyzed using the conclusion shown in Fig. 15(c).

4.4 Three-Dimensional Flow Structure

To explain the complex flow field laws generated by self-propulsion, we adopted the q criterion (Borazjani and Sotiropoulos 2008) to intercept the contour of the 3D vortex structure, which was visualized in solid blue. The q criterion can effectively distinguish the vortex and static zones, and help analyze the complex fluid dynamics during advancement. The value of q is defined as $q = 0.5(\|\Omega\|^2 - \|S\|^2)$, where S and Ω represent the symmetric and asymmetric segments of the velocity gradient, respectively. Figure 16 shows the 3D vorticity structure of the swimmer in the homologous mode based on different views. The distribution of a row of main vortex streets and a row of auxiliary vortex streets are revealed. The auxiliary vortex streets are sandwiched between the main vortex streets in a complex dotted star shape and are distributed parallelly along the x -axis. This is a special accessory in the double-tentacled movement

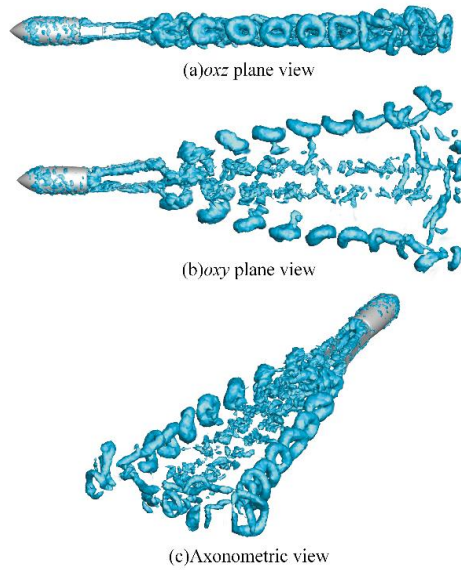


Fig. 16. Vorticity isosurfaces of the homologous mode.

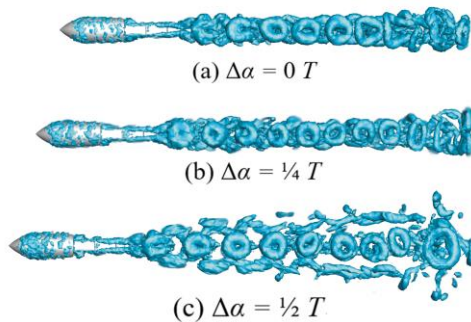


Fig. 17. Comparison of different modes based on the vortex structure in the oxz plane.

mode, and its main cause is that the newly produced wake vortex is compressed and divided by space. The characteristics of the auxiliary vortex streets demonstrate the uniqueness of the double-tentacled model. The flow pattern of the main vortex streets is similar to that of the previous vortex streets related to autonomous fish swimming (Borazjani and Sotiropoulos 2010; Xia *et al.* 2015), showing a fan-shaped divergence comprising several symmetrical sickle-shaped vortices on the left and right sides.

Figure 17 shows the vortex structures of the three driving modes in the oxz plane; the front view of the sickle vortex is similar to a swimming ring. Owing to the difference in the final linear velocity of the three driving behaviors in the steady state, the distances of adjacent swimming loop-shaped vortices also differ. The auxiliary vortex streets of the first two driving behaviors can be covered by the main vortex streets in this view. However, the auxiliary vortex streets of the reverse mode diverges along both sides in the oxz plane. Although the energy loss of the partially dispersed vortex in this plane is inevitable, the reverse mode remains the ideal energy protector.

5. CONCLUSION

A double-tentacled swimmer with a multijoint system that can realize three self-driving modes was proposed in this paper. We systematically distinguished the kinematic logic of the three modes and analyzed their pros and cons based on the time history of the hydrodynamic parameters and the quantitative influence of the kinematic parameters. The main findings are summarized as follows:

(1) The convergence trends of the asymptotic average curves of the three modes are similar, and their main difference is reflected in the amplitude of the fluctuation peaks and the staggering law. Under the same parameters, the reverse mode is better than the other two modes, its startup acceleration is faster and its final steady-state velocity coefficient (C_U) is higher. This phenomenon is attributed to the rationality of energy distribution of the reverse mode, reflecting the characteristics of high explosiveness.

(2) The definition of the swing frequency (f) and the maximum pitch angle (θ_{\max}) are invaluable in the analysis of the superimposed effects of self-propulsion in the three driving modes. An increase in both effectively improves the propulsion effect, but the small spanwise space limits the value of the θ_{\max} of the single joint in the interlace and reverse modes. However, the homologous mode has better spanwise flexibility compared with the other two, which raises the upper limit of the propulsive performance of double-tentacled swimmer without considering its stability.

(3) The three modes produces regular vortex street patterns downstream, including two rows of the main vortex streets distributed on both sides and two rows of auxiliary vortex streets sandwiched in between. The vortex street shape distribution of the homologous and reverse modes is completely axisymmetric in shape, and the interlace mode is influenced by the law of cross-swinging, causing the distance and phase differences between the vortex pairs on the left and right sides. We believe that the interlace mode produces uncontrollable lateral displacement, resulting in a deviation of the travel path, and is thus not the best driving choice for self-propulsion.

In summary, we numerically constructed a dual-actuated swimmer with a multijoint system and examined the advantages and disadvantages of multiple driving modes under self-propulsion. The results of this novel cooperative mechanism indicate that double tentacles equipped on swimmers are like a pair of vortex generators, and in terms of biohydrodynamic analogy, they operate more efficiently than the traditional fish-like robot in the BCF mode. Note that the present double-tentacled collaborative study is limited to linear advancement. In the future, it is necessary to study the laws of 3D motion, including steering and pitching, to pave the way for the physical research of AUVs.

ACKNOWLEDGEMENTS

This work was supported by National Natural Science Foundation of China [grant number 51875101], and State Key Laboratory of Robotics and System (HIT) [grant number SKLRS-2018-KF-11]. The authors greatly appreciate the referees for their helpful comments and suggestions, which help improve this paper.

REFERENCES

- Acharya, T. and L. Casimiro (2020). Evaluation of flow characteristics in an onshore horizontal separator using computational fluid dynamics. *Journal of Ocean Engineering and Science* 5(3), 261-268.
- Anderson, E. J. and M. A. Grosenbaugh (2005). Jet flow in steadily swimming adult squid. *Journal of Experimental Biology* 208(6), 1125-1146.
- Borazjani, I. and F. Sotiropoulos (2008). Numerical investigation of the hydrodynamics of carangiform swimming in the transitional and inertial flow regimes. *Journal of Experimental Biology* 211(10), 1541-1558.
- Borazjani, I. and F. Sotiropoulos (2010). On the role of form and kinematics on the hydrodynamics of self-propelled body/caudal fin swimming. *Journal of Experimental Biology* 213(1), 89-107.
- Borazjani, I., F. Sotiropoulos, E. D. Tytell and G. V. Lauder (2012). Hydrodynamics of the bluegill sunfish C-start escape response: Three-dimensional simulations and comparison with experimental data. *Journal of Experimental Biology* 215(4), 671-684.
- Carling, J., T. L. Williams and G. Bowtell (1998). Self-propelled anguilliform swimming: Simultaneous solution of the two-dimensional Navier-Stokes equations and Newton's laws of motion. *Journal of Experimental Biology* 201(23), 3143-3166.
- Carrica, P. M., A. M. Castro and F. Stern (2010). Self-propulsion computations using a speed controller and a discretized propeller with dynamic overset grids. *Journal of Marine Science and Technology* 15(4), 316-330.
- Carrica, P. M., R. V. Wilson, R. W. Noack and F. Stern (2007). Ship motions using single-phase level set with dynamic overset grids. *Computers and Fluids* 36(1), 1415-1433.
- Coelho, R. C. V., N. A. M. Araujo and M. M. Telo da Gama (2020). Propagation of active nematic-isotropic interfaces on substrates. *Soft Matter* 16(17), 4256-4266.
- Dong, G. and X. Lu (2005). Numerical analysis on the propulsive performance and vortex shedding of fish-like travelling wavy plate. *International Journal for Numerical Methods in Fluids* 48(12), 1351-1373.
- Doustdar, M. M. and H. Kazemi (2019). Effects of fixed and dynamic mesh methods on simulation of stepped planing craft. *Journal of Ocean Engineering and Science* 4(1), 33-48.
- Duman, S. and S. Bal (2019). A quick-responding technique for parameters of turning maneuver. *Ocean Engineering* 179(5), 189-201.
- Feilich, K. L. and G. V. Lauder (2015). Passive mechanical models of fish caudal fins: Effects of shape and stiffness on self-propulsion. *Bioinspiration and Biomimetics* 10(3), 036002.
- Feng, Y., Y. Su, H. Liu and Y. Su (2020). Numerical simulation of a self-propelled fish-like swimmer with rigid and flexible caudal fins. *Journal of Environmental Biology* 3(2), 54-67.
- Fetherstonhaugh, S. E. A. W., Q. Shen and O. Akanyeti (2021). Automatic segmentation of fish midlines for optimizing robot design. *Bioinspiration and Biomimetics* 16(4), 046005.
- Guo, S., K. Sugimoto, S. Hata, J. Su and K. Oguro (2000). A new type of underwater fish-like microrobot. *IEEE International Conference on Intelligent Robots and Systems* 2, 867-872.
- Jiang, W., Y. Zhang and A. Yang (2019). Numerical simulations of complex aircraft configurations using structured overset grids with implicit hole-cutting. *Aerospace Science and Technology* 94, 105402.
- Kern, S. and P. Koumoutsakos (2006). Simulations of optimized anguilliform swimming. *Journal of Experimental Biology* 209(24), 4841-4857.
- Lee, J. and D. You (2013). An implicit ghost-cell immersed boundary method for simulations of moving body problems with control of spurious force oscillations. *Journal of Computational Physics* 233(1), 295-314.
- Leroyer, A. and M. Visonneau (2005). Numerical methods for RANSE simulations of a self-propelled fish-like body. *Journal of Fluids and Structures* 20(7), 975-991.
- Li, N., J. Zhuang, Y. Zhu, G. Su and Y. Su (2021). Fluid dynamics of a self-propelled biomimetic underwater vehicle with pectoral fins. *Journal of Ocean Engineering and Science* 6(2), 160-169.
- Liao, P., S. Zhang and D. Sun (2018). A dual caudal-fin miniature robotic fish with an integrated oscillation and jet propulsive mechanism. *Bioinspiration and Biomimetics* 13(3), 036007.
- Liu, B., S. Zhang, F. Qin and J. Yang (2014). Fluid-structure interaction study on the performance of flexible articulated caudal fin. *Advanced Robotics* 28(24), 1665-1676.
- Liu, G., S. Liu, Y. Xie, D. Leng and G. Li (2020). The Analysis of Biomimetic Caudal Fin Propulsion Mechanism with CFD. *Applied Bionics and Biomechanics*, 1-11.
- Moreira, D., N. Mathias and T. Morais (2020). Dual

- flapping foil system for propulsion and harnessing wave energy: A 2D parametric study for unaligned foil configurations. *Ocean Engineering* 215(12), 107875.
- Ohashi, K., T. Hino, H. Kobayashi, N. Onodera and N. Sakamoto (2019). Development of a structured overset Navier-Stokes solver with a moving grid and full multigrid method. *Journal of Marine Science and Technology* 24(3), 884-901.
- Olcay, A. B., M. T. Malazi, A. Okbaz, H. Heperkan, E. Firat, V. Ozbolat, H. Heperkan, E. Firat, V. Ozbolat, M. G. Gokcen, B. Sahin (2017). Experimental and numerical investigation of a longfin inshore squid's flow characteristics. *Journal of Applied Fluid Mechanics* 10(1), 21-30.
- Park, Y. J., U. Jeong, J. Lee, S. R. Kwon, H. Y. Kim and K. J. Cho (2012). Kinematic condition for maximizing the thrust of a Robotic Fish using a compliant caudal fin. *IEEE Transactions on Robotics* 28(6), 1216-1227.
- Rahman, M. M., Y. Toda and H. Miki (2011). Computational Study on a Squid-Like Underwater Robot with Two Undulating Side Fins. *Journal of Bionic Engineering* 8(1), 25-32.
- Roper, D. T., S. Sharma, R. Sutton and P. Culverhouse (2011). A review of developments towards biologically inspired propulsion systems for autonomous underwater vehicles. *Proceedings of the Institution of Mechanical Engineers Part M: Journal of Engineering for the Maritime Environment* 225(2), 77-96.
- Schultz, W. W. and P. W. Webb (2002). Power requirements of swimming: Do new methods resolve old questions? *Integrative and Comparative Biology* 42(5), 1018-1025.
- Seo, J. H. and R. Mittal (2011). A sharp-interface immersed boundary method with improved mass conservation and reduced spurious pressure oscillations. *Journal of Computational Physics* 230(19), 7347-7363.
- Sfakiotakis, M., D. M. Lane and J. B. C. Davies (1999). Review of fish swimming modes for aquatic locomotion. *IEEE Journal of Oceanic Engineering* 24(2), 237-252.
- Singh, N., A. Gupta and S. Mukherjee (2019). A dynamic model for underwater robotic fish with a servo actuated pectoral fin. *SN Applied Sciences* 1(7), 1-9.
- Singh, Y., S. K. Bhattacharyya and V. G. Idichandy (2017). CFD approach to modelling, hydrodynamic analysis and motion characteristics of a laboratory underwater glider with experimental results. *Journal of Ocean Engineering and Science* 2(2), 90-119.
- Su, G., H. Shen, N. Li, Y. Zhu and Y. Su (2021). Numerical investigation of the hydrodynamics of stingray swimming under self-propulsion. *Journal of Fluids and Structures* 106, 103383.
- Suebsaiprom, P. and C. L. Lin (2015). Maneuverability modeling and trajectory tracking for fish robot. *Control Engineering Practice* 45, 22-36.
- Wang, J. and D. Wan (2020). CFD study of ship stopping maneuver by overset grid technique. *Ocean Engineering* 197(1), 106895.
- Wu, Z., J. Yu, M. Tan and J. Zhang (2014). Kinematic comparison of forward and backward swimming and maneuvering in a self-propelled sub-carangiform robotic fish. *Journal of Bionic Engineering* 11(2), 199-212.
- Wynn, R. B., V. A. I. Huvenne, T. P. Le Bas, B. J. Murton, D. P. Connelly, B. J. Bett, H. A. Ruhl, K. J. Morris, J. Peakall, D. R. Parsons, E. J. Sumner, S. E. Darby, R. M. Dorrell, J. E. Hunt (2014). Autonomous Underwater Vehicles (AUVs): Their past, present and future contributions to the advancement of marine geoscience. *Marine Geology* 352, 451-468.
- Xia, D., Q. Yin, Z. Li, W. Chen, Y. Shi and J. Dou (2021). Numerical study on the hydrodynamics of porpoising behavior in dolphins. *Ocean Engineering* 229(4), 108985.
- Xia, D., W. Chen, J. Liu and X. Luo (2018). The energy-saving advantages of burst-and-glide mode for thunniform swimming. *Journal of Hydrodynamics* 30(6), 1072-1082.
- Xia, D., W. Chen, J. Liu, Z. Wu and Y. Cao (2015). The three-dimensional hydrodynamics of thunniform swimming under self-propulsion. *Ocean Engineering* 110(12), 1-14.
- Xie, O., B. Li and Q. Yan (2018). Computational and experimental study on dynamics behavior of a bionic underwater robot with multi-flexible caudal fins. *Industrial Robot* 45(2), 267-274.
- Xu, Y. and D. Wan (2012). Numerical simulation of fish swimming with rigid pectoral fins. *Journal of Hydrodynamics* 24(2), 263-272.
- Yang, L., Y. Su, Q. Xiao (2011). Numerical Study of Propulsion Mechanism for Oscillating Rigid and Flexible Tuna-Tails. *Journal of Bionic Engineering* 8(4), 406-417.
- Yu, J., C. Zhang and L. Liu (2016). Design and control of a single-motor-actuated robotic fish capable of fast swimming and maneuverability. *IEEE/ASME Transactions on Mechatronics* 21(3), 1711-1719.
- Yu, J., L. Wang and M. Tan (2007). Geometric optimization of relative link lengths for biomimetic robotic fish. *IEEE Transactions on Robotics* 23(2), 382-386.
- Zhang, S., Y. Qian, P. Liao, F. Qin and J. Yang (2016). Design and Control of an Agile Robotic Fish with Integrative Biomimetic Mechanisms. *IEEE/ASME Transactions on Mechatronics* 21(4), 1846-1857.